Available online at www.sciencedirect.com
ScienceDirect
Trans. Nonferrous Met. Soc. China 35(2025) 2918−2934
Transactions of Nonferrous Metals Society of China
www.tnmsc.cn

Structural characteristics, tensile properties and room-temperature high-cycle fatigue properties of heterogeneous structure in near-α titanium alloys

Ji-fei HU[1], Peng QI[2], Wu WEI[1], Bo-long LI[1], Tong-bo WANG[2], Jia-ming YIN[3], Zuo-ren NIE[1]

1. Key Laboratory of Advanced Functional Materials, Ministry of Education, Beijing University of Technology, Beijing 100124, China;
2. Chinalco Research Institute of Science and Technology Co., Ltd., Beijing 102209, China;
3. Aerospace Research Institute of Materials & Processing Technology, Beijing 100076, China

Received 20 January 2024; accepted 14 November 2024

Abstract: A heterogeneous structure composed of elongated primary α and secondary α grains with a size of 670 nm was produced by subjecting the bimodal microstructure of a titanium alloy to hot rolling, annealing, and aging treatments. This heterogeneous structure exhibited significantly improved strength owing to a combination of heterogeneous deformation-induced strengthening and dislocation strengthening. A short-duration high-temperature heat treatment facilitated a synergistic enhancement of yield strength and elongation at both room temperature and 650 °C. The fracture elongation at room temperature and 650 °C increased by 36.7% and 130.4%, respectively, compared with that of bimodal microstructure. The stacking of geometrically necessary dislocations with a single slip system at the phase boundary and the longer effective slip length of the dislocations are the reasons for the significant improvement in elongation. The elongated primary α phase in lamellar bimodal microstructure, composed of multiple primary α grains, has better resistance to the anti-fatigue crack initiation effect.

Key words: titanium alloys; heterostructures; ductility; high-temperature deformation; heterogeneous deformation-induced strengthening

1 Introduction

Near-α titanium alloys have garnered significant research interest owing to their exceptional specific strength, high-temperature performance, and corrosion resistance [1,2]. However, achieving a synergistic enhancement in room and high temperatures (particularly at 650 °C [2]) performances remains a significant challenge. The equiaxed microstructure exhibits a low strength at both room and high temperatures [3−5]. Conversely, a lamellar microstructure exhibits reduced elongation at room temperature [6]. Both equiaxed and lamellar microstructures possess inherent limitations that impede their widespread application. The bimodal microstructure (BM) is widely used because of its balanced mechanical properties at room and high temperatures [7,8]. Nevertheless, their room-temperature elongation is lower than that of the equiaxed microstructure, and their high-temperature strength is lower than that of the lamellar microstructure. Developing titanium alloys that exhibit exceptional performance at room and high temperatures (650 °C) presents a formidable challenge [9]. Researchers continue to

Corresponding author: Wu WEI, Tel: +86-15901158170, E-mail: weiwu@bjut.edu.cn;
Zuo-ren NIE, Tel: +86-10-67391536, E-mail: zrnie@bjut.edu.cn
https://doi.org/10.1016/S1003-6326(25)66857-9
1003-6326/© 2025 The Nonferrous Metals Society of China. Published by Elsevier Ltd & Science Press
This is an open access article under the CC BY-NC-ND license (http://creativecommons.org/licenses/by-nc-nd/4.0/)

explore novel microstructure models to improve their reliability in high-temperature environments.

Grain refinement has been a well-established approach for strengthening metals. Ultrafine-grained (UFG) alloys exhibit exceptional strength; however, their low elongation severely limits their practical application [10−15]. In recent years, multiple reports have highlighted the significant role of heterogeneous structures, such as heterogeneous lamellar structure [10], ultralight steel with a dual-heterogeneous-structure [16], and ferrite/martensite laminated steels [17], which have proven to be instrumental in achieving the synergistic improvement in both strength and ductility. These structures are formed through a deformation process, incorporating a combination of elongated coarse and fine grains. Such heterogeneously structured materials exhibit heterogeneous deformation-induced (HDI) strengthening effects during deformation [16−23]. Nevertheless, the fine grains in these heterostructures significantly reduce their high-temperature strength. This phenomenon is the primary limitation hindering the application of heterostructures at elevated temperatures. Consequently, the development of high-temperature resistant heterostructures is challenging.

High-cycle fatigue behavior in titanium alloys has been a subject of significant research interest. During high-cycle fatigue, the amplitude of stress is lower than the yield strength, and crack initiation is primarily driven by local stress concentrations caused by the microstructure. Therefore, the microstructure plays a critical role in the fatigue failure response of alloys [24]. The fatigue crack initiation of BM usually occurs at the interface between the primary α (α_p) phase and secondary α (α_s) phase or the α_p/α_p grain boundary [25]. Planar dislocation slip is more pronounced in α_p grains, and these planar slip bands appearing on the surface can act as the starting position of fatigue crack initiation. Crack initiation often occurs preferentially on the α_p side [26,27]. The lamellar structure cracks fracture along and through the lamellar path. Compared with the BM, the main crack propagation path in the lamellar structure is more tortuous and has a stronger anti-fatigue crack propagation ability [28,29]. These findings indicate that the microstructure has a dominant effect on the initiation and propagation of microcracks in the material.

Currently, there is little work on the heterogeneous structure of near-α titanium alloys. The aim of this study is to report novel methods for preparing heterogeneous structures and investigate the influence of heterogeneous structures on tensile properties and room-temperature high-cycle fatigue properties. We have achieved a significant improvement in toughness (fracture elongation increased by 36.7% and 130.4%) at both room temperature and 650 °C without compromising the strength by designing heterostructures in near-α titanium alloys compared with the BM, i.e., forming a 17% elongated α_p/α_s lamellar bimodal microstructure (LBM), and thus promotes delamination, microstructural toughening, delayed initiation of high-cycle fatigue cracks at room temperature. The near-α titanium alloy with LBM was realized by subjecting the initial structure to hot rolling and well-designed heat treatment processes. Various characterization methods were used to elucidate the mechanism of formation and the process of the microstructure evolution. The load−unload−reload (LUR) test was used to confirm the strengthening mechanisms. The fatigue crack initiation behavior, microcrack initiation location, and dislocation slip type of the LBM were discussed.

2 Experimental

2.1 Material preparation

A Ti−5.7Al−3.2Sn−5.4Zr−0.5Mo−1.0Nb−0.4Si−0.2Er (wt.%) alloy ingot with a diameter of 200 mm and a length of 140 mm was produced using the vacuum arc remelting (VAR) technology three times. The $\beta/(\alpha+\beta)$ transus-temperature of the titanium alloy was 1005 °C, as measured using differential scanning calorimetry. The ingot was initially forged at 1150 °C to obtain a cubic billet with a cross-section of 50 mm. This step was followed by a second forging step at 980 °C to obtain a rectangular billet with a cross-sectional side length of 40 mm [30]. The processing of titanium alloy involves two sequential steps. The first step was to obtain a BM titanium alloy. The forged bar was solution-treated at 990 °C for 1 h to generate the BM with the equiaxed α_p phase. The second step was to obtain the hot-rolled microstructure by hot rolling in the α phase region of the solution-treated titanium alloy. The BM sheets were annealed at a specific temperature for

15 min. During hot rolling, a reduction of 15% per pass was implemented, followed by 5 min annealing after each pass. This rolling process was repeated eight times, resulting in a total rolling reduction of 73%.

2.2 Microstructural characterization

Scanning electron microscope (SEM, Quanta FEG 650), electron backscatter diffraction (EBSD), and JEM−2010F transmission electron microscope (TEM) were used to observe the metallographic structure and microstructure. The scanning step of EBSD was 0.14 μm. The SEM samples were finely ground with sandpaper, polished, and etched. The etching solution was 3 vol.% HF + 5 vol.% HNO_3 + 92 vol.% H_2O.

2.3 Tensile tests

Tensile samples with dimensions of 3 mm in thickness and 55 mm in gauge length were cut along the rolling direction (RD) in the sheet. Tensile testing was performed at room temperature. Tensile tests were performed on a universal testing machine. Cyclic LUR tensile tests were performed with the above tensile equipment. Apply a constant loading rate (1×10^{-3} s^{-1}) to the sample until reaching a fixed strain (e.g. 1%), then unload it to 20 MPa, followed by reapplying the next fixed strain (e.g. 2%), and then unload it to 20 MPa, to realize cyclic loading and unloading test.

2.4 Fatigue experiment

Before the room temperature fatigue experiment, we determined different fatigue maximum stress based on tensile tests. The axial high cycle fatigue test of titanium alloy was carried out on the MTS810-50 fatigue testing machine. The maximum stress of high cycle fatigue at room temperature was set as 520, 550 and 580 MPa by stress control. The loading waveform was a sine wave, the stress ratio R was 0.1, and the loading frequency was 100 Hz. The surface of the sample was polished to eliminate the influence of machining on the surface damage and fatigue life of the sample.

3 Results

3.1 Initial BM

The alloy underwent a forging process, followed by heat treatment at 990 °C for 1 h to form the BM, as shown in Fig. 1. This BM functioned as the precursor for subsequent processing steps. The α_p exhibited an equiaxed morphology and comprised 17% of the microstructure. The α_s consisted of fine platelets and constituted the remaining 83% of the microstructure. The inverse pole figure (IPF) maps revealed random crystallographic orientations in the BM. The grain size, characterized by the equivalent circle diameter, followed a normal distribution with an average grain size of 7.74 μm.

3.2 Characteristics of α-heterogeneous-structure (α-HS) and LBM

Through multiple 15% hot rolling processes, the initial equiaxed α_p phase grains were elongated along the RD. These elongated α_p grains exhibited a

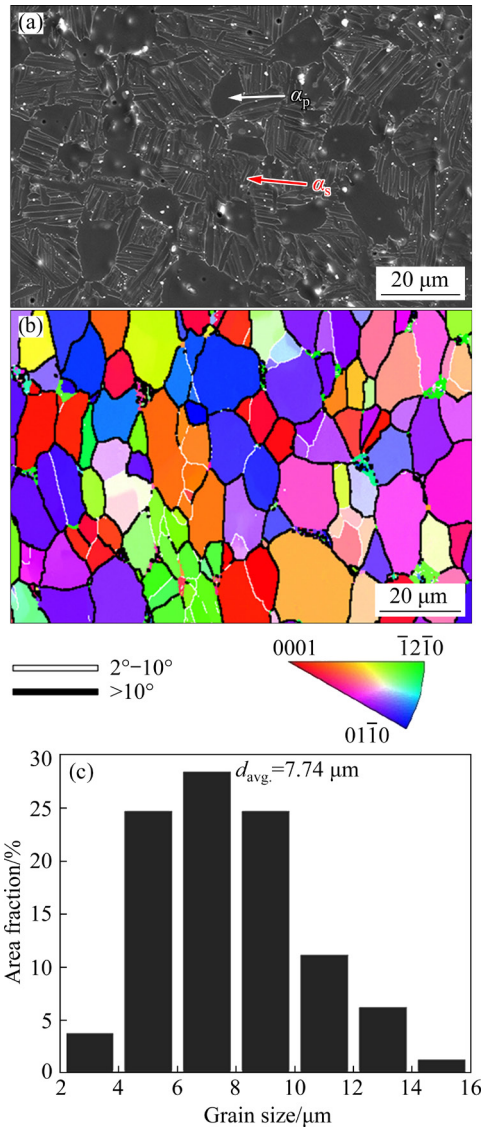

Fig. 1 SEM image (a) and IPF map (b) of BM, and grain size distribution (c)

high density of dislocations within the grains. The length of these grains ranged from 20 to 50 μm, with a thickness of approximately 3 μm. The α_s grains underwent recovery to maintain the hard UFG structure. The hot-rolling process in the single-phase region introduced a high density of defects within the microstructure. In this heterogeneous microstructure, α_s grains experience multiaxial stress. Under the multiaxial strain components and coexistence of soft α_p and hard α_s phases, significant grain refinement occurred. This process maintained a high elongation by retaining the large-sized α_p grains (the α_p phase content was 17%). While the α_p phase in the LBM still exhibits a lamellar morphology (Fig. 2(g)), its interior is composed of a series of equiaxed α_p grains, as highlighted by the white dashed box in Fig. 2(h). The length of these α_p phases ranged within 15−50 μm, with a thickness of 5 μm. The α_s phase was transformed back into a lamellar morphology via a short-duration high-temperature treatment in the (α+β) phase region (990 °C, 20 min, air cooling (AC)). During this process, α_s transformed into the β phase before the α_p phase [31]. The 20 min of duration ensured the complete phase transformation of the α_s phase, while the α_p phase underwent incomplete recrystallization. Notably, the α_s grains exhibited significant difference owing to different heat treatment methods.

The kernel average misorientation (KAM) maps of the three microstructures are presented in Figs. 2(c, f, i). The KAM map reflects the density of geometrically necessary dislocations (GNDs) in the alloy. The average KAM values were 1.12×10^{14}, 9.8×10^{13}, and 3.3×10^{13} m^{-2}. The hot-rolled microstructure exhibited the highest density of GNDs, with a lower density in the α_p phase. The density of GNDs in the recovered α_p phase in α-HS decreased significantly, while the density in the α_s phase remained relatively unchanged. The density of GNDs in the α_s phase in LBM decreases sharply after phase-transformation treatment. However, a certain density of GNDs persisted, which were primarily located at the grain boundaries. Similarly,

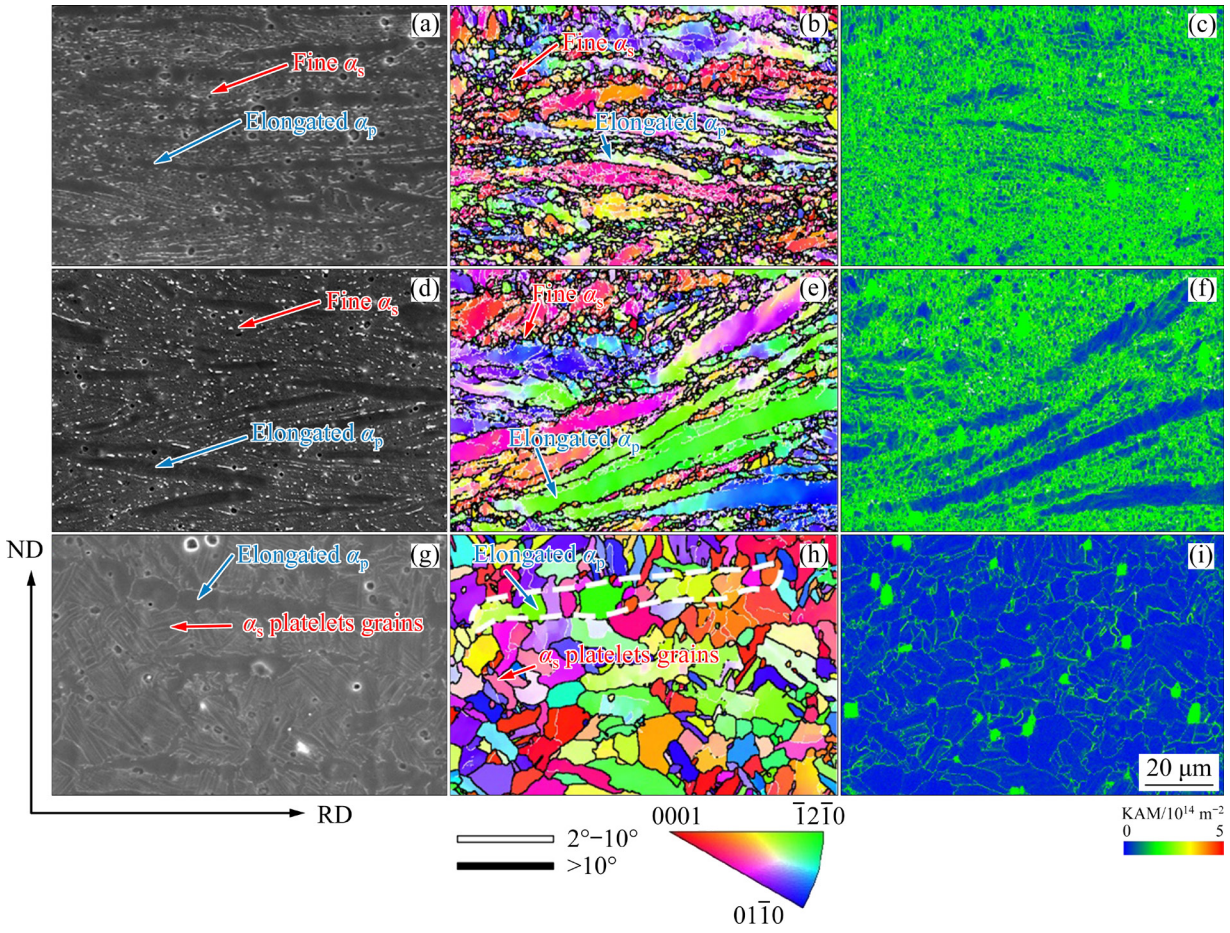

Fig. 2 SEM images (a, d, g), IPF maps (b, e, h) and KAM maps (c, f, i) of titanium alloys: (a−c) Hot-rolled microstructure; (d−f) α-HS; (g−i) LBM

the α_p phase in the LBM, having undergone incomplete recrystallization, also retained a certain density of GNDs at the grain boundary. These observations show that the density of GNDs in the microstructure can be greatly reduced by short-term phase transformation treatment (990 °C, 20 min, AC), and the stabilization and aging treatment at low temperatures have limited effect on eliminating dislocations.

The grain size distributions of hot-rolled microstructure, α-HS, and LBM are shown in Figs. 3(a1, b1, c1), respectively. Following the heat treatment, the α-HS exhibited minimal changes in grain size; it was characterized by the presence of UFG α_s grains and micron-sized α_p grains. In the LBM, the α_s and α_p grains exhibited similar grain sizes, comparable to those observed in the BM. However, the overall grain size in the LBM was small. To study the effect of deformation on the texture formation of the overall phase, the α_p and α_s phases were separately analyzed. The results indicate a dominant texture in the α_p phase, with the texture intensity as high as 42.26. Conversely, the texture intensity of the α_s phase is only 13.66, showing random texture. These observations indicate that the α_p phase bears the major deformation during the rolling process, while the α_s phase undergoes grain refinement. The texture strength of the α-HS decreased slightly compared to that of the hot-rolled state, and the trend was the same as that of the rolled state. However, the texture strength of the LBM was only 8.6, indicating a random texture [32].

In the α-HS, the α_s grains underwent a recovery process to maintain the hard UFG structure [10] (Figs. 4(b, c)). Notably, the refined α_s grain size was comparable to that of the original platelet boundary width of the α_s grain (Figs. 4(c, f)), with a size of approximately 500 nm. This finding indicates that the refinement of α_s grains occurred along the platelet boundary inside the grains, resulting in a loss of their original plate-like morphology. Consequently, the grain size of the α_s grains in the α-HS depended on the original platelet boundary width of the α_s grain in the BM. The hot-rolling process conducted in the single-phase α region introduced a high density of defects. In this heterogeneous microstructure, α_s grains experienced multiaxial stress. Under the combined influence of multiaxial strain components and the coexistence of soft α_p and hard α_s phases, significant grain refinement occurred. WANG et al [33] reported that limited dislocation storage efficiency in UFG materials leads to a rapid decline

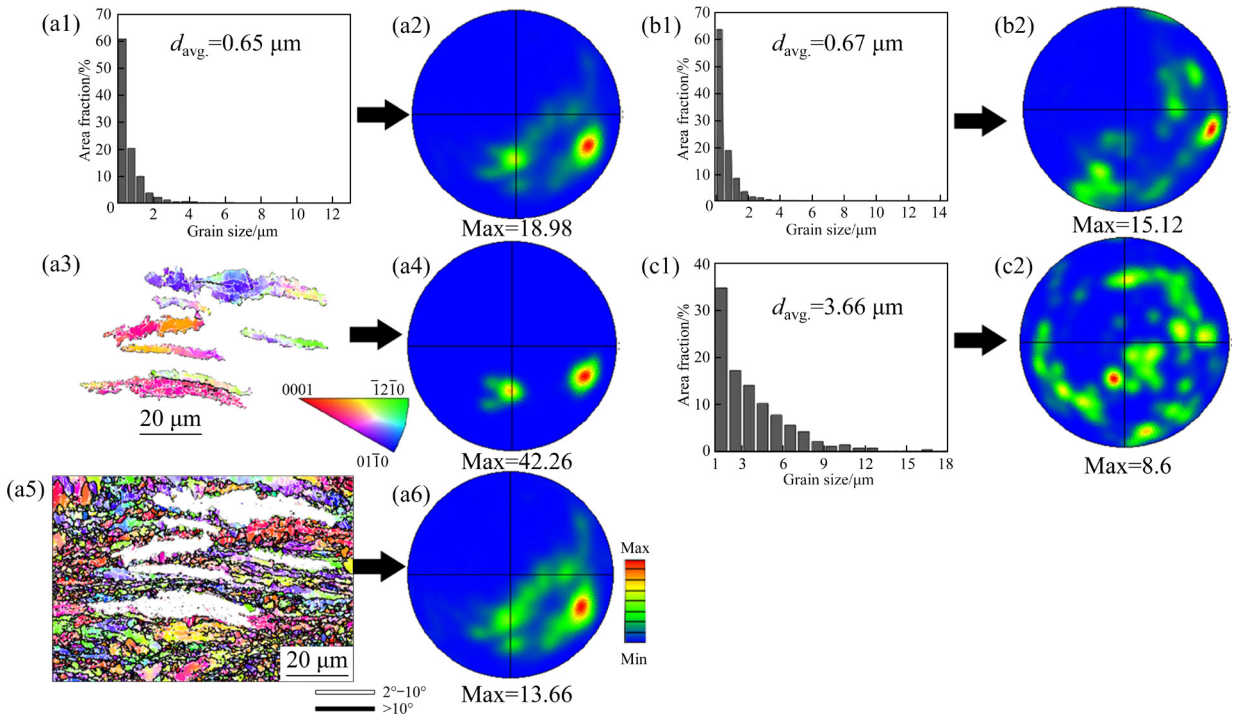

Fig. 3 Grain size distributions of hot-rolled microstructure (a1), α-HS (b1) and LBM (c1), IPF maps of α_p (a3) and α_s (a5) phases, and pole figures (PFs) of α_p+α_s (a2, b2, c2), α_p (a4) and α_s (a6) phases

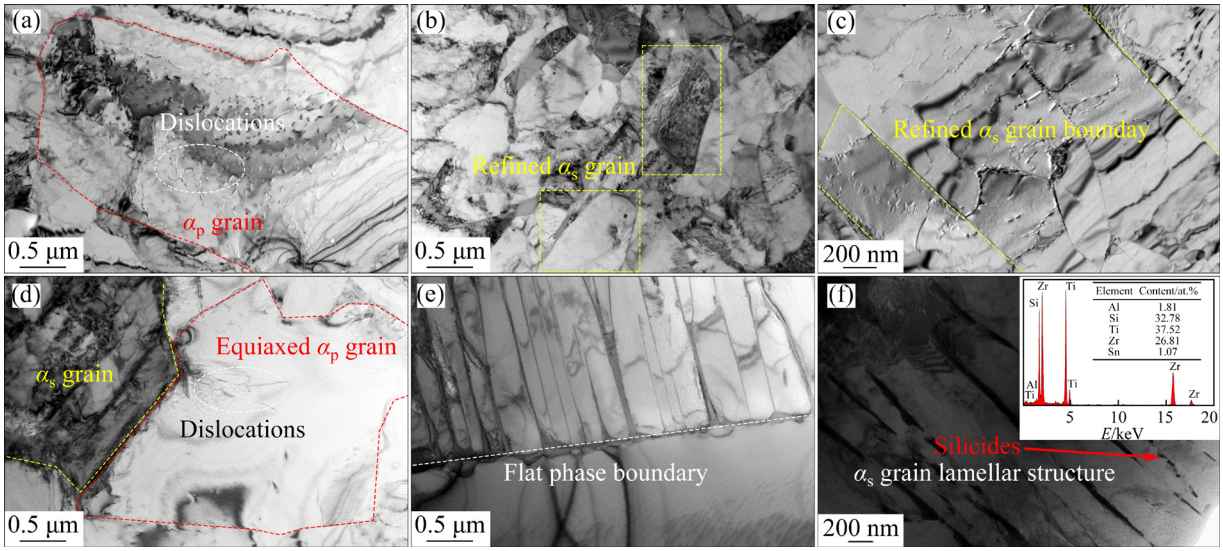

Fig. 4 (a) Elongated α_p grains of α-HS; (b) Broken α_s grains of α-HS; (c) Broken α_s grains boundary of α-HS; (d) Equiaxed α_p grains of LBM; (e) Interface boundary between α_p and α_s of LBM; (f) α_s platelets and silicide following phase transformation of LBM

in the work-hardening effect during deformation. Consequently, such high-strength materials typically exhibit low elongation unless larger grains with appropriate sizes and volume fractions are incorporated [33]. To address this limitation, this study employed the strategy of retaining the large-sized α_p grains (the α_p phase content was 17%) to maintain a high elongation in the final material.

In the LBM, the α_p grains that underwent recrystallization exhibited a low density of dislocations or were essentially free from dislocations (Fig. 4(d)). The α_s phase was transformed back into the lamellar morphology via a short-duration high-temperature treatment conducted in the $\alpha+\beta$ phase region (990 °C, 20 min, AC). During this process, the α_s phase transformed into the β phase before the transformation of the α_p phase [31]. Notably, the α_s grains exhibited significant variations owing to the differences in the employed heat treatment methods. Figure 4(f) shows the structure of the α_s grains, revealing their internal composition of platelets. The fusiform silicide observed along the α_s platelets was identified as the $(Ti,Zr)_6Si_3$ phase based on its characteristic morphology and energy dispersive X-ray spectroscopy (EDS) analysis [34]. Figure 4(e) shows that α_s grains have recovered to a plate-like morphology following the phase transformation. The α_p grains are situated at the flat phase boundaries. This phase boundary is the demarcation between the α_p and α_s phases, and between the two grain types (soft and hard grains and grains with different sizes) in the heterogeneous structure.

3.3 Tensile properties

Compared with the initial BM, the α-HS exhibited higher yield strength (1024 MPa), while maintaining a comparable fracture elongation (15%). Notably, the α-HS can significantly enhance the room-temperature strength; however, it exhibited a noticeable decrease in high-temperature strength accompanied by a significant increase in elongation. This observation aligned with the primary focus of most heterogeneous-structure materials with room-temperature performance [3,10,22]. To address the challenge of reduced high-temperature strength in the α-HS, we implemented a novel heat treatment process (LBM). This process aimed to achieve a synergistic improvement in both yield strength and fracture elongation, particularly focusing on enhancing the high-temperature fracture elongation from 23% to 53%. Additionally, the room-temperature fracture elongation also reached 20%. As illustrated in Figs. 5(b) and (d), α-HS and LBM exhibited performances that transcended the conventional strength−ductility trade-off observed in other titanium alloys [3]. They demonstrated exceptionally high fracture elongation at both room and elevated temperatures.

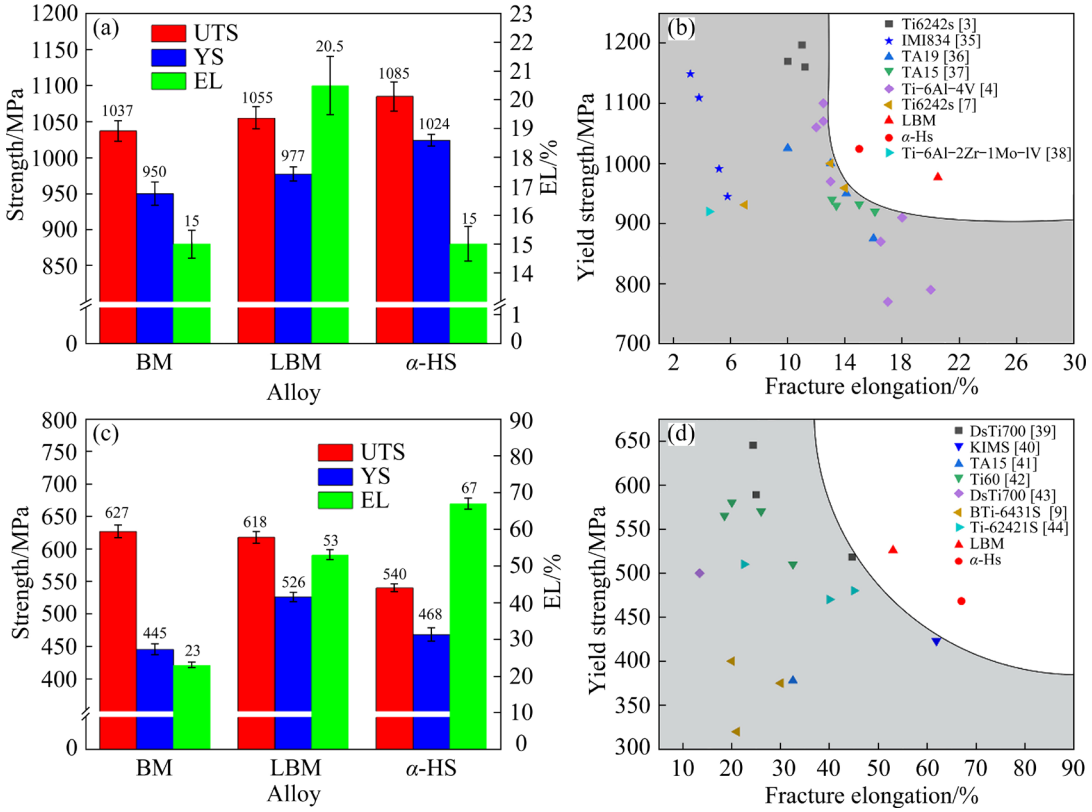

Fig. 5 (a) Tensile properties at room temperature; (b) Tensile properties of α-HS and LBM with typical titanium alloys [3,4,7,35−38] at room temperature; (c) Tensile properties at high-temperature (650 °C); (d) Tensile properties of α-HS and LBM with typical titanium alloys at 600 or 650 °C [9,39−44]

3.4 Heterogeneous deformation-induced (HDI) strengthening effect

To elucidate the underlying mechanisms behind the exceptional mechanical behavior observed in heterogeneously structured materials, the contribution of the HDI strengthening effect was investigated using the LUR tests. These tests enabled the quantification of the Bauschinger effect and HDI stress on the strength of the material [16−23,45,46]. In BM, α-HS, and LBM, we observed significant hysteresis loops, with larger hysteresis loops indicating a stronger Bauschinger effect and higher HDI stress. In other words, in heterogeneously structured materials, the presence of soft and hard phases leads to strain gradients under stress. These strain gradients led to the formation of a high density of GNDs near the boundaries, ultimately resulting in HDI strengthening. HDI stress (σ_{HDI}) was calculated using the following equation [45]:

$$\sigma_{HDI}=\frac{\sigma_u+\sigma_r}{2}$$

where σ_u is the unloading yield stress, and σ_r is the reloading yield stress.

As shown in Fig. 6, before necking, the HDI stress of the material increased with an increase in strain, particularly in the early stage of strain, where the HDI stress increased more significantly. In the initial stage of the BM and LBM, the HDI stress was relatively low, partly because of the low dislocation density within the grains and the low accumulation of GNDs at the phase boundary. In contrast, the α-HS exhibited a comparatively high HDI stress in the initial stage. As testing continued, GNDs continued to accumulate, leading to an increase in the HDI stress. Additionally, the relatively similar grain sizes of α_p and α_s in BM and LBM resulted in a lower HDI stress compared with that in the α-HS. In the case of HS, the significant difference in grain sizes leads to a more pronounced HDI strengthening effect, which is the primary cause for the higher peak HDI stress observed in the α-HS. Additionally, the higher density of GNDs in the α-HS is the main reason for the higher HDI stress in the early stage of strain. Furthermore,

compared to the work of ZHOU et al [3], this study completed a large number of LUR test cycles, which is closely associated with a significant improvement in elongation. Similarly, in the later stages of testing, premature fractures occurred because of the continuous accumulation of dislocations during the LUR testing.

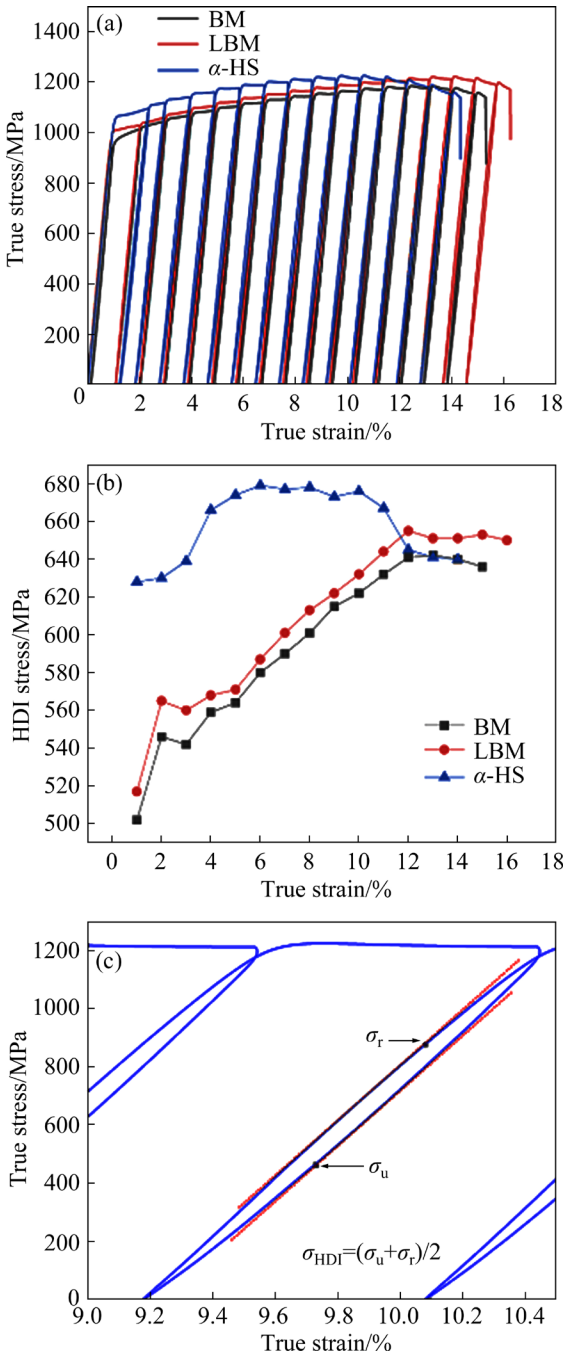

Fig. 6 Contribution of Bauschinger effect and HDI strengthening: (a) Tensile LUR true stress versus true strain curves; (b) Evolution of HDI stress with true strain; (c) Measured hysteresis loops at unloading strain of 10% with definitions of σ_r and σ_u

3.5 Effect of microstructure on high-cycle fatigue properties at room temperature

High-cycle fatigue tests were conducted on BM and LBM at room temperature to evaluate their room-temperature fatigue performances. The fatigue strength of titanium is approximately 50% of its tensile strength. The maximum stress levels of 520, 550, and 580 MPa were chosen for the room-temperature high-cycle fatigue tests. The stress−number curves of BM and LBM at room temperature are shown in Fig. 7. The fit lines in Fig. 7 were obtained using the least squares method. The results indicate that the room temperature high-cycle fatigue strengths (10^7 cycles) of BM and LBM are 521 MPa and 559 MPa, respectively, the room temperature fatigue strength of LBM being 38 MPa higher than that of BM. The fatigue strength to tensile strength ratios of BM and LBM are 50.2% and 53.0%, indicating that LBM has significantly improved high-cycle fatigue performance compared to BM.

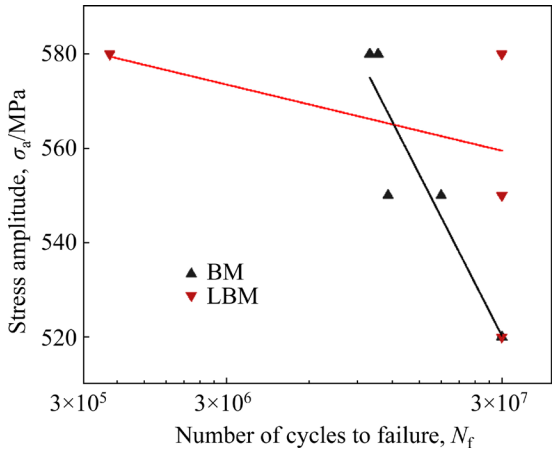

Fig. 7 Stress−number curves for BM and LBM at room temperature

Figure 8 shows the high-cycle fatigue fracture morphology of BM fractured under the maximum loading stress of 550 MPa. It was found that the alloy fractures were divided into fatigue crack initiation, crack propagation, and transient fracture zones. Notably, only a single site for high-cycle fatigue crack initiation was observed. The fatigue crack initiation zone was observed at high magnification, and fatigue facets were found on the subsurface of the alloy, as shown in Fig. 8(b). Therefore, a single crack source was initiated at the subsurface of the alloy. The formation of these fatigue facets is due to the dislocation motion

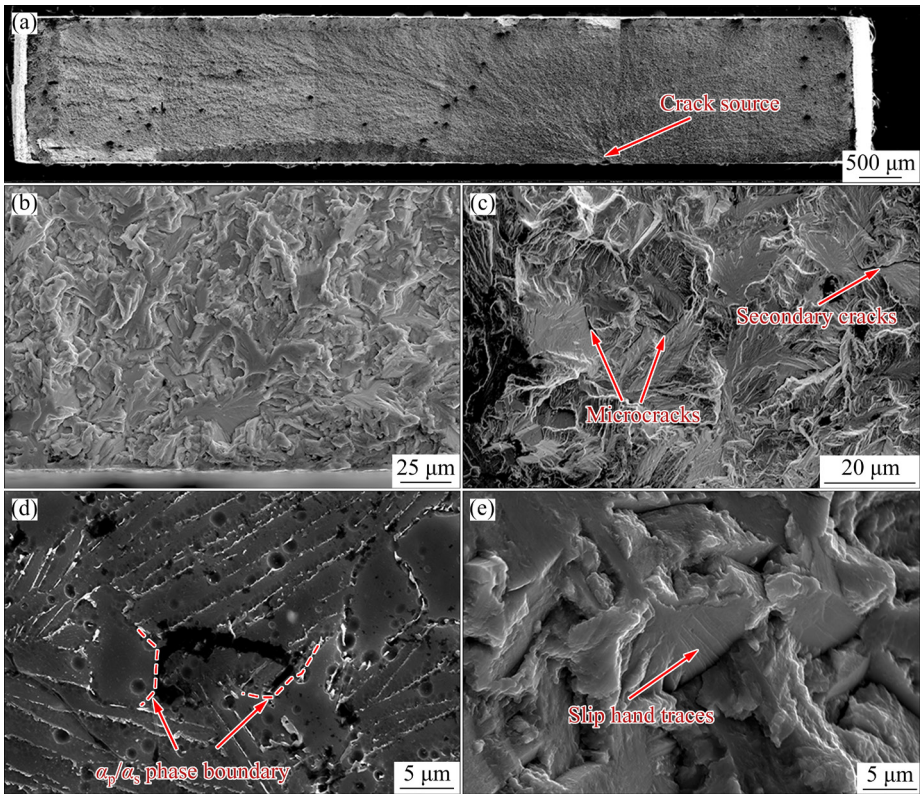

Fig. 8 High-cycle fatigue fracture morphology of BM at room-temperature under 550 MPa: (a) General view of fractured surface; (b) Fatigue crack initiation zone; (c, d) Microcracks on fracture surface and fracture section, respectively; (e) Slip band traces in fatigue crack propagation zone

dominated by the plane slip in the α_p phase at the initial stage of cyclic loading. With the continuous cyclic loading, the α_p phase in the BM has a large dislocation slip path. The α_p/α_s boundary begins to present dislocation accumulation along the dislocation plane of the slip surface, resulting in stress concentration and initiation of microcracks. These microcracks gradually separated along the specific slip surface, ultimately forming a small fatigue facet. Figures 8(c) and (d) show the presence of microcracks that initiate along the α_p/α_s boundary on both fracture surfaces and fracture sections. These observations indicate that the primary location for high-cycle fatigue crack initiation in the BM at room temperature is the α_p/α_s boundary.

Figure 9 shows the high-cycle fatigue fracture morphology of the LBM fractured under a maximum loading stress of 580 MPa. Only a single fatigue crack source was observed. The fractured surface morphology was divided into fatigue crack initiation, crack propagation, and instantaneous fracture zones. The fatigue surface is located on the subsurface region of the alloy (Fig. 9(b)). At the fatigue crack initiation zone in the LBM, microcracks were initiated at the α_p/α_s and α_p/α_p boundaries. These microcracks subsequently propagated along the α_p boundary. These observations indicated that the room-temperature high-cycle fatigue cracks in the LBM were primarily initiated along the α_p boundary.

4 Discussion

4.1 Formation mechanism of heterogeneous structure in titanium alloys

Figure 10 illustrates the heat treatment processes and corresponding microstructural evolution of various microstructures. During the rolling process, the presence of both soft and hard phases in BM led to uneven deformation. Under a single 15% deformation, the α_p grains elongated along the rolling direction, while the α_s grains underwent substantial grain fragmentation and refinement. This fragmentation severely disrupted the plate-like morphology of the α_s grains, resulting in the formation of the aforementioned rolling state microstructure.

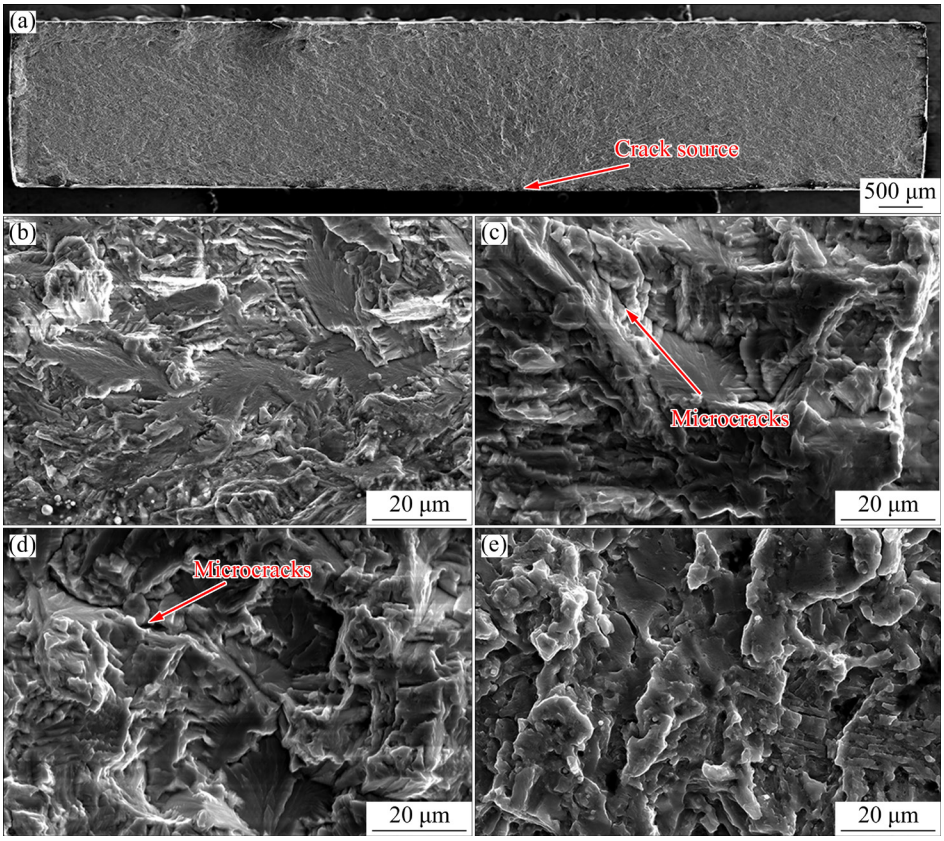

Fig. 9 High-cycle fatigue fracture morphology of LBM at room temperature under 580 MPa: (a) General view of fractured surface; (b) Fatigue crack initiation zone; (c) Fatigue crack propagation zone; (d) Microcrack propagated along α_p boundary; (e) Microcrack fracture surface

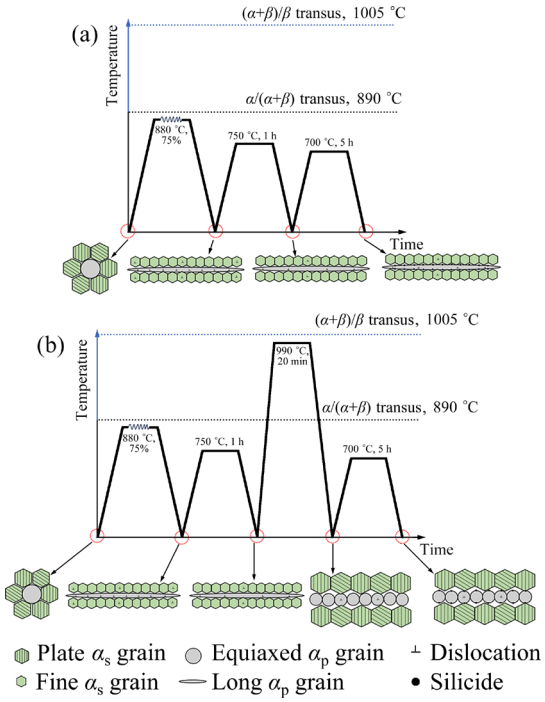

Fig. 10 Schemes of microstructure evolution during heat treatment, illustrating formation mechanism of heterogeneous structure: (a) α-HS; (b) LBM

Based on the BM, we designed two distinct processes. The first process, as shown in Fig. 10(a), is a rolling and heat treatment. In this process, the rolling temperature was chosen at the upper limit of the single-phase α region (880 °C). In this single-phase region, no phase transformation occurred, making it easier to control and maintain a constant α_p phase content. Additionally, this process suppressed dynamic recrystallization during rolling, resulting in a more pronounced elongation of the α_p grains and refinement of the α_s grains. A subsequent annealing treatment (750 °C, 1 h, AC) was employed to eliminate some of the dislocations and internal stresses generated during rolling. This step prevented the storage of excessive deformation energy during the next step of the short-duration phase-transformation process, which led to excessive grain equalization of α_p grains. The short-duration high-temperature treatment (990 °C, 20 min, AC), in conjunction with the phase transformation of the titanium alloy, ensured the complete transformation of refined α_s grains into

grains with lamellar morphology. Simultaneously, this treatment refined the large, elongated α_p grains into small α_p grains and aligned them along the RD. This part needs to be coordinated with the annealing treatment to achieve the desired effect. Finally, the aging treatment of (700 °C, 5 h, AC) promotes the precipitation of silicides and other phases near the phase boundaries and within the α_p and α_s grains. This aging treatment is a well-established process.

4.2 Influence of heterogeneous structure on tensile properties

In the α-HS, where small grains of α_s surround large grains of α_p, the hardness difference between α_s and α_p regions is exacerbated, resulting in α_p being softer and α_s being harder. Under tensile loading, dislocations preferentially nucleate in the α_p phase [3]. Compared with equiaxed α_p grains, elongated α_p grains are more likely to maintain planar slip. On the one hand, this is due to the elongation direction of α_p grains being parallel to the loading direction (LD), on the other hand, due to the HCP structure of α-Ti having few slip systems, which increases the difficulty of dislocation glide plane changes [47]. This results in the accumulation of dislocations with the same slip plane at phase boundaries, where their stress fields superimpose, thereby generating back stresses on the α_p side and forward stresses on the α_s side, leading to significant HDI stresses [47]. Many years ago, due to an insufficient understanding of HDI strengthening, researchers regarded this extra hardening as back stress, which is not comprehensive. Therefore, researchers now commonly refer to this extra hardening as HDI strengthening [22].

Under tensile loading, the soft α_p phase in heterogeneous structure deformed first [3]. However, the surrounding smaller and harder α_s phase acts as a constraint during deformation, impeding further deformation of the soft α_p phase. This constraint led to the accumulation of dislocations at the α_p/α_s phase boundaries, thereby generating HDI stresses. These HDI stresses impeded the subsequent movement of dislocations in the α_p phase, necessitating high stresses for yielding to occur. This phenomenon ultimately enhanced the yield strength of the heterogeneous structure [3,46−50]. Notably, in this study, the boundaries in the heterogeneous structure encompassed not only the α_p/α_s phase boundary but also the boundary between large grains (α_p grains) and small grains (α_s grains). By adjusting the rolling and subsequent heat-treatment processes, the composite boundary was formed between these two phases or grain sizes. In the α-HS, dislocations in the α_p phase slip led to a more pronounced accumulation of GNDs at the composite boundaries. This phenomenon significantly increased the HDI stress, thereby enhancing strength and elongation and contributing to the higher dislocation density. While this high dislocation density strengthened the material, it could also counteract the improvement in elongation, resulting in a similar elongation as that in the BM. Conversely, the accumulation of GNDs at the phase boundaries in LBM was weaker, resulting in a significantly lower HDI stress compared with that in α-HS. However, a significant improvement in elongation was achieved owing to the lower dislocation density [51].

Figure 11 shows the SEM and TEM images of the fractured surfaces of BM and LBM under tensile stress. In the BM, the α_p phase exhibited significant elongation along the LD, with the grain width decreasing from 7.7 to 4.1 μm. This observation indicated a continuous elongation of the α_p grains during the tensile deformation accompanied by a progressive change in crystallographic orientation. Numerous crystal orientations aligned with the LD, facilitating the continuous generation of new slip systems. Ultimately, this process led to the formation of dislocation cells at phase boundaries (Fig. 11(b)). In contrast, the α_p phase in the LBM maintained a width of 5 μm before and after the tensile deformation, indicating a superior resistance to high-temperature deformation. Because of the pre-existing alignment of the LD with the RD, the α_p grains in the LBM experienced minimal changes in crystallographic orientation during the stretching process. This limitation restricted the activation of new slip systems, resulting in a predominant slip of dislocations along a single slip system parallel to the LD at the phase boundaries (Figs. 11(d, e)). The slip process was further impeded by the presence of grain boundaries and silicide precipitates. Consequently, dislocations from these single slip systems accumulated at the phase boundaries, resulting in the formation of GNDs accumulations (Fig. 11(f)). Notably, as reported in previous studies

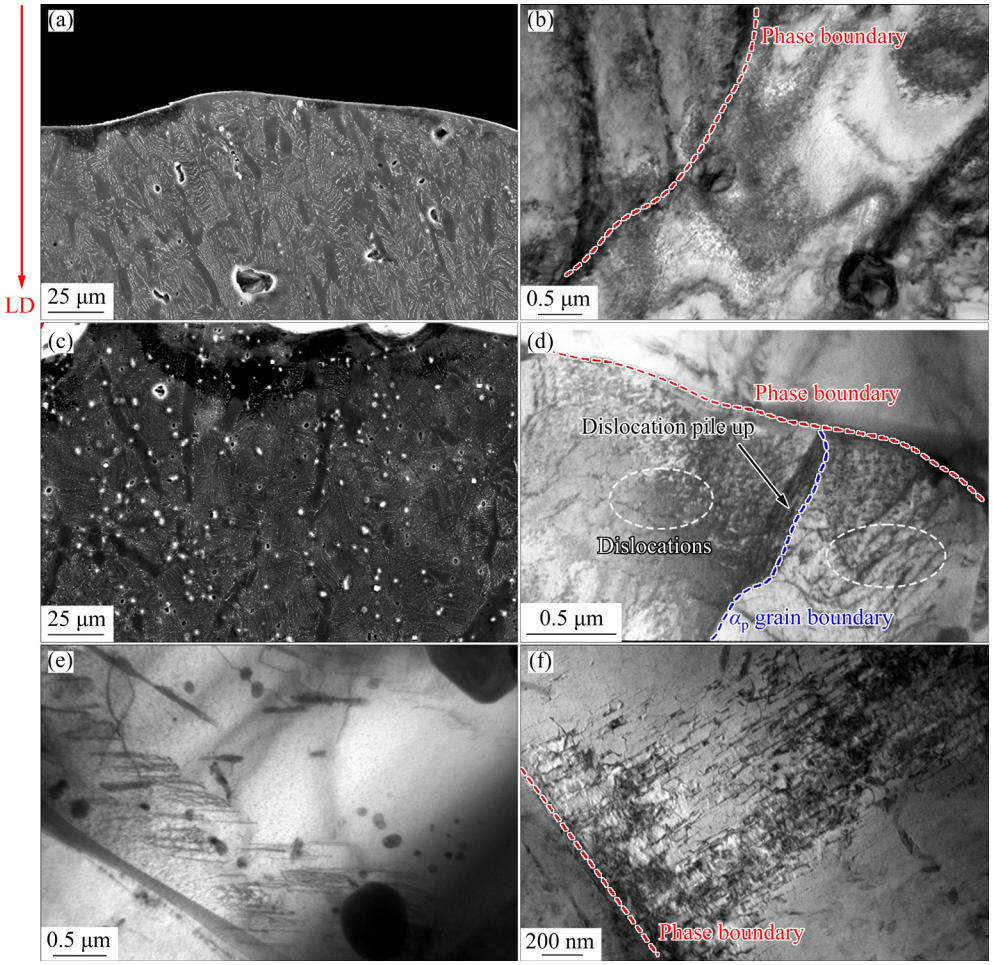

Fig. 11 Microstructure and dislocation behavior near tensile fracture (necking zone) at 650 °C: (a) SEM image of BM; (b) Structure of dislocation cell at phase boundary of BM; (c) SEM image of LBM; (d) Inhibitory effect of α_p grain boundaries on dislocation movement of LBM; (e) Image of dislocation pinned by silicide precipitate along grain boundary of LBM; (f) Accumulation of GNDs on slip plane in front of phase boundary of LBM

on heterogeneous structures, the stacking of GNDs generated from single slip systems is more pronounced than those arising from multiple or mixed slip systems [47]. This observation indicates that the HDI strengthening effect remains significant, contributing to improvements in high-temperature yield strength and fracture elongation, particularly enhancing the latter property.

In the BM, the α_p grains exhibited an equiaxed morphology, resulting in a short effective slip length for dislocations [36,52]. Additionally, the poor geometric compatibility between α_p and α_s phases hindered slip transfer across these boundaries. This incompatibility promoted significant dislocation entanglement at the phase boundaries, further impeding elongation improvement. In contrast, in the LBM, α_p phase was composed of a series of α_p grains, offering good geometric compatibility that facilitated slip transfer, particularly at high temperatures. This enhanced compatibility significantly increased the effective slip length of dislocations and minimized stress concentration at the phase boundaries [36]. These factors promoted improved elongation without compromising strength owing to the presence of the small-sized α_p grains [53].

4.3 Influence of microstructure on high-cycle fatigue properties at room temperature

To elucidate the microscopic mechanisms of the initiation of fatigue crack in the BM, we conducted a detailed characterization of the dislocation structure near the main fatigue crack of the material using TEM. Two-beam diffraction under the condition $g \cdot b=0$ was employed to determine the Burgers vector and slip surface of the dislocations. Figure 12 reveals the presence of numerous straight dislocations slip lines in α_p and α_s

phases after the high-cycle fatigue deformation at room temperature. Two-beam diffraction was performed on the selected areas to assess dislocation visibility under specific diffraction vectors: $[1\bar{1}01]$, $[2\bar{1}\bar{1}0]$ and $[0\bar{1}12]$. If the dislocation was invisible under the $[0\bar{1}12]$ condition but visible under the other conditions, its Burgers vector was $1/3[\bar{2}110]$. Conversely, if the dislocation was invisible under $[1\bar{1}01]$ conditions but visible under other conditions, the Burgers vector was $1/3[11\bar{2}0]$. This two-beam analysis indicates that the extensive parallel slip lines originated from the prismatic slip activated by the $\langle a\rangle$ type dislocations, because the prismatic slip in the α phase of titanium alloy is known to be more readily activated during deformation [54]. During the initial stage of deformation, dislocations were preferentially activated at the α_p/β_{trans} boundary and $\alpha_s/\beta_{residual}$ boundaries owing to the significant disparity in the structure and active slip systems between the α and the residual β phases, as shown in Fig. 12(c). As the number of loading cycles increased, the pronounced difference in critical shear stress between various dislocation slip systems at room temperature promoted the initiation of single dislocation slip in titanium alloy. Additionally, the shear of ordered Ti_3Al precipitates further facilitated the planar slip of dislocations, forming numerous parallel slip lines in the α_p phase. With the progressive increase in dislocation density in the α_p phase, dislocation pile-ups were formed at the α_p/α_s boundary. These pile-ups led to stress concentrations that triggered the initiation of fatigue microcracks at the α_p/α_s boundary. Furthermore, the slip surfaces of the dislocations promoted the initiation and propagation of these fatigue cracks.

Figure 13 illustrates the dislocation structure of LBM after high-cycle fatigue deformation at room temperature. The observations reveal the following characteristics of dislocation motion. First, the dislocation motion in the α_p and α_s phases was primarily mediated by the planar slip mechanism. Two-beam diffraction analysis confirmed that this slip was predominantly prismatic slip activated by the $\langle a\rangle$-type dislocations with a Burgers vector of $[11\bar{2}0]$. Second, parallel dislocation lines originating from the $\beta_{residual}$ phase were observed. Thirdly, dislocation pile-up occurred at the α_p/α_p and α_p/α_s boundaries, as shown in Figs. 13(b, c). In summary, the room-temperature

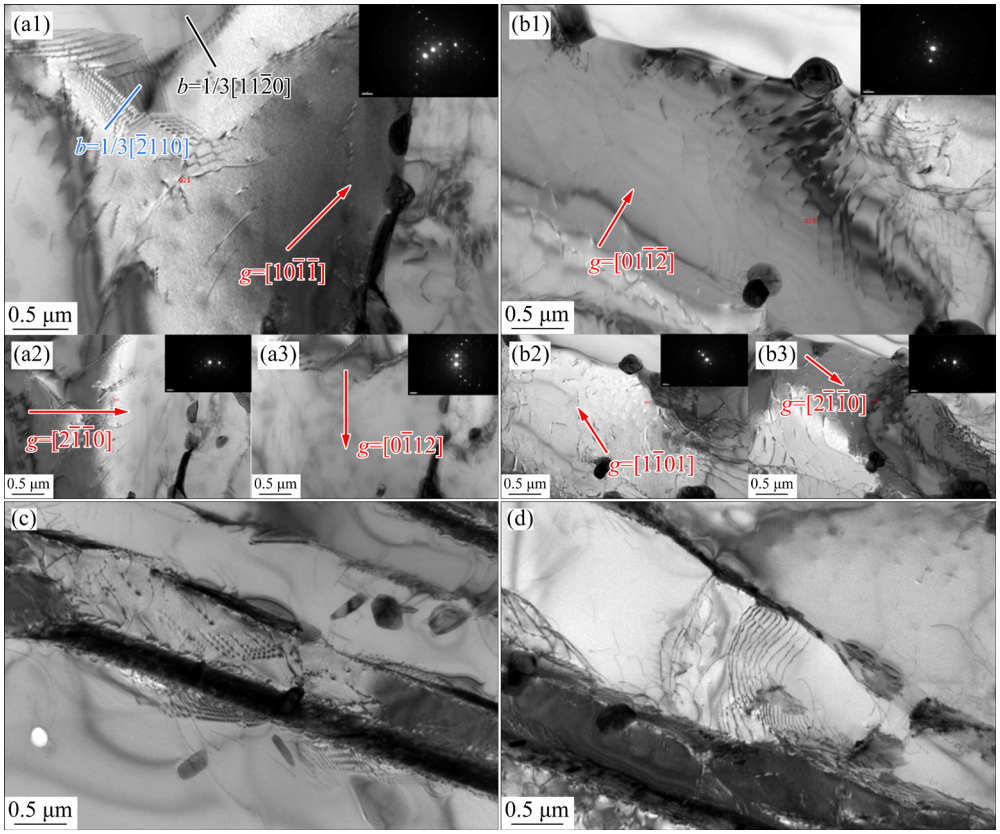

Fig. 12 Microstructures of BM near main crack after room-temperature high-cycle fatigue fracture: (a1−a3, b1−b3) α_p phase; (c, d) α_s phase

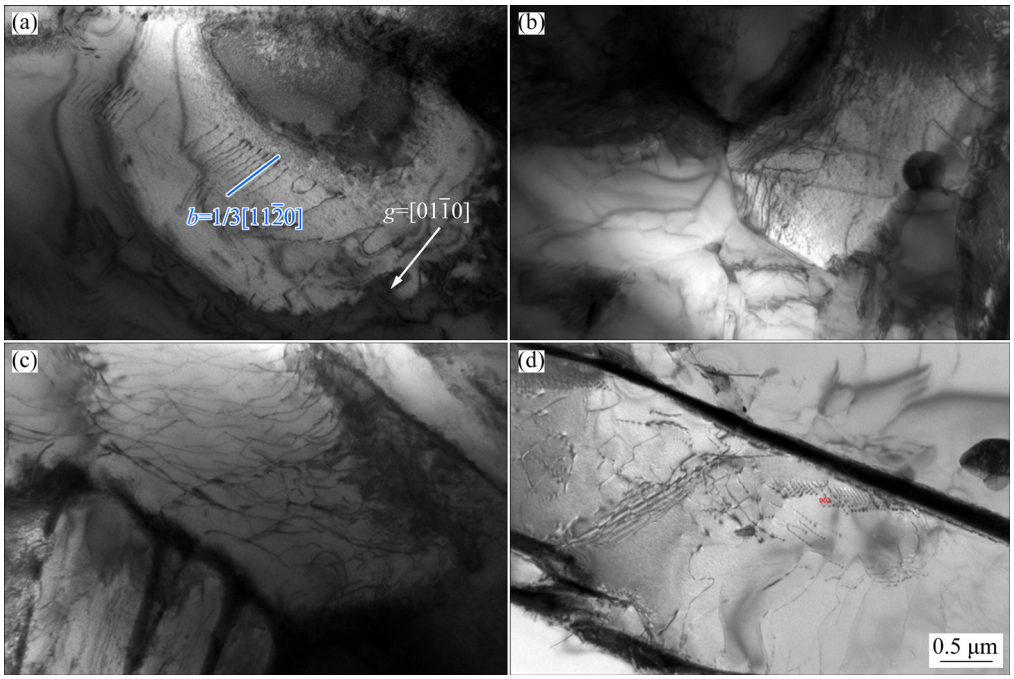

Fig. 13 Microstructures of LBM near main crack after room-temperature high-cycle fatigue fracture: (a) α_p phase; (b, c) Dislocation pile-ups at grain boundary and α_p/α_s boundary, respectively; (d) α_s phase

high-cycle fatigue crack initiation behavior and underlying microscopic dislocation mechanism in BM and LBM exhibited fundamental similarities. Both materials experienced stress concentrations at the α_p phase boundaries owing to the prismatic slip of dislocations, resulting in fatigue crack initiation and propagation along specific slip planes. However, the fine grain size in the LBM, and alignment of the α_p grains in a straight line along the loading direction influenced the dislocation behavior. The shorter slip path in a single grain in the LBM compelled dislocations to traverse multiple α_p grains before accumulating at the α_p/α_s phase boundary, significantly delaying pile-up formation. And LBM exhibited a high lattice strength. Consequently, LBM demonstrated superior resistance to fatigue crack initiation, resulting in a high room-temperature high-cycle fatigue strength.

The LBM is a special case of BM, which exhibited the following characteristics: (1) The α_p phase exhibited a layered morphology and comprised multiple α_p grains aligned along the RD; (2) The plate-like α_s phase effectively constrained the α_p phase. These characteristics of the LBM contributed to its superior mechanical properties: (1) The layered characteristics of LBM facilitated the accumulation of GNDs on a single slip plane in front of the boundary. This stacking configuration represented the most effective mode for the accumulation of GNDs, thereby strengthening the materials; (2) The elongated morphology of the α_p phase enhanced its stability at elevated temperatures compared to the equiaxed α_p phase observed in BM; (3) The elongated α_p phase exerted a stronger constraint on the α_s phase compared to the equiaxed α_p phase in the BM. This significant constraint can influence the mechanical behavior of the microstructure.

The α-HS exhibited distinct features compared to the BM, contributing significantly to its enhanced room-temperature strength. These features arose from the morphological and size differences between the α_p and α_s phases: (1) The α_p phase exhibited a lamellar morphology, lacking the equiaxed α_p grains in the phase along the RD; (2) The α_s grains were significantly refined and lacked prominent lamellar characteristics; (3) The fine α_s phase effectively constrained the α_p phase.

5 Conclusions

(1) Compared to the initial alloy with BM, the near-α titanium alloy with heterogeneous structure (α-HS) exhibited a significant increase in room-

temperature strength (YS: 1024 MPa) without compromising elongation (15%). The observed high strength was primarily attributed to the contribution of HDI stresses.

(2) The near-α titanium alloy with lamellar bimodal microstructure (LBM) achieved high strength and exceptional fracture elongation at both room temperature (YS: 977 MPa, EL: 20.5%) and 650 °C (YS: 526 MPa, EL: 53%). Compared to the initial alloy with BM, the significant enhancement in high-temperature elongation could be attributed to the stacking of GNDs with a single slip system at the phase boundary and the longer effective slip length of the dislocations.

(3) In the LBM, the primary mode of dislocation motion during high-cycle fatigue was prismatic slip mediated by the $\langle a \rangle$-type dislocation. The phase boundaries were the primary sites for microcrack initiation. Notably, the elongated α_p phase composed of multiple α_p grains exhibited superior resistance to fatigue crack initiation.

CRediT authorship contribution statement

Ji-fei HU: Investigation, Methodology, Formal analysis, Writing – Original draft, Writing – Review & editing; **Peng QI:** Methodology, Investigation; **Wu WEI** and **Bo-long LI:** Supervision, Funding acquisition, Writing – Review & editing; **Tong-bo WANG** and **Jia-ming YIN:** Methodology, Investigation; **Zuo-ren NIE:** Supervision, Funding acquisition, Writing – Review & editing.

Declaration of competing interest

The authors declare that they have no known competing financial interests or personal relationships that could have appeared to influence the work reported in this paper.

Data availability

Data will be made available on request.

Acknowledgments

The authors are grateful to the National Key Research and Development Program of China (Nos. 2021YFB3704202, 2021YFB3704205), R&D Program of Beijing Municipal Education Commission, China (No. KM 202110005010), Beijing Natural Science Foundation, China (No. 2202009), National Natural Science Foundation of China (No. 51621003), Basic Research Program of Jiangsu Province, China (No. BK20191148).

References

[1] BANERJEE D, WILLIAMS J C. Perspectives on titanium science and technology [J]. Acta Materialia, 2013, 61: 844−879.

[2] ZHAO Hong-ze, LU Bin, TONG Min, YANG Rui. Tensile behavior of Ti−22Al−24Nb−0.5Mo in the range 25−650 °C [J]. Materials Science and Engineering: A, 2017, 679: 455−464.

[3] ZHOU Yu, WANG Ke, WEN Xin, XIN Ren-long, WANG Jing-feng, LIU Qing. Achieving synergy enhancement of strength and ductility in Ti−6Al−2Sn−4Zr−2Mo−0.1Si alloy by fabricating a new multiscale microstructure [J]. Scripta Materialia, 2023, 226: 115233.

[4] CHONG Yan, DENG Guan-yu, GAO Si, YI Jang-ho, SHIBATA A, TSUJI N. Yielding nature and Hall−Petch relationships in Ti−6Al−4V alloy with fully equiaxed and bimodal microstructures [J]. Scripta Materialia, 2019, 172: 77−82.

[5] ZHANG Zhi-xiong, QU Shou-jiang, FENG Ai-han, SHEN Jun. Achieving grain refinement and enhanced mechanical properties in Ti−6Al−4V alloy produced by multidirectional isothermal forging [J]. Materials Science and Engineering: A, 2017, 692: 127−138.

[6] SARKAR R, MUKHOPADHYAY A, GHOSAL P, NANDY T K, RAY K K. Effect of aged microstructure on the strength and work hardening behavior of Ti−15V−3Cr−3Sn−3Al alloy [J]. Metallurgical and Materials Transactions A, 2015, 46: 3516−3527.

[7] HOSSEINI R, MORAKABATI M, ABBASI S M, HAJARI A. Development of a trimodal microstructure with superior combined strength, ductility and creep-rupture properties in a near alpha titanium alloy [J]. Materials Science and Engineering: A, 2017, 696: 155−165.

[8] LI Shi-kai, XIONG Bai-qing, HUI Song-xiao, YE Wen-jun, YU Yang. Comparison of the fatigue and fracture of Ti−6Al−2Zr−1Mo−1V with lamellar and bimodal microstructures [J]. Materials Science and Engineering: A, 2007, 460/461: 140−145.

[9] ZHANG Wen-jing, SONG Xiao-yun, HUI Song-xiao, YE Wen-jun, WANG Wei-qi. Phase precipitation behavior and tensile property of a Ti−Al−Sn−Zr−Mo−Nb−W−Si titanium alloy [J]. Rare Metals, 2015, 37: 1064−1069.

[10] WU Xiao-lei, YANG Mu-xin, YUAN Fu-ping, WU Gui-lin, WEI Yu-jie, HUANG Xiao-xu, ZHU Yun-tian. Heterogeneous lamella structure unites ultrafine-grain strength with coarse-grain ductility [J]. Proceedings of the National Academy of Sciences of the United States of America, 2015, 112: 14501−14505.

[11] VALIEV R Z, ALEXANDROV I V. Nanostructured materials from severe plastic deformation [J]. Nanostructured Materials, 1999, 12: 35−40.

[12] LANGDON T G. Twenty-five years of ultrafine-grained materials: Achieving exceptional properties through grain refinement [J]. Acta Materialia, 2013, 61: 7035−7059.

[13] VALIEV R Z, ALEXANDROV I V, ZHU Yun-tian, LOWE T C. Paradox of strength and ductility in metals processed by

severe plastic deformation [J]. Journal of Materials Research, 2002, 17: 5−8.

[14] VALIEV R. Nanostructuring of metals by severe plastic deformation for advanced properties [J]. Nature Materials, 2004, 3: 511−516.

[15] ZHU Yun-tian, LIAO Xiao-zhou. Nanostructured metals-Retaining ductility [J]. Nature Materials, 2004, 3: 351−352.

[16] GENG Xiao-xiao, GAO Jun-heng, HUANG Yu-he, WANG Shui-ze, ZHANG Yu, WU Gui-lin, ZHAO Hai-tao, WU Hong-hui, MAO Xin-ping. A novel dual-heterogeneous-structure ultralight steel with high strength and large ductility [J]. Acta Materialia, 2023, 252: 118925.

[17] CAO Wen-quan, ZHANG Ming-da, HUANG Chong-xiang, XIAO Shu-yang, DONG Han, WENG Yu-qing. Ultrahigh Charpy impact toughness (~450 J) achieved in high strength ferrite/martensite laminated steels [J]. Scientific Reports, 2017, 7: 41459.

[18] HUANG Chong-xiang, WANG Yan-fei, MA Xiao-long, YIN Sheng, HÖPPEL H W, GÖKEN M, WU Xiao-lei, GAO Hua-jian, ZHU Yun-tian. Interface affected zone for optimal strength and ductility in heterogeneous laminate [J]. Materials Today, 2018, 21: 713−719.

[19] YANG Mu-xin, YAN Ding-shun, YUAN Fu-ping, JIANG Ping, MA E, WU Xiao-lei. Dynamically reinforced heterogeneous grain structure prolongs ductility in a medium-entropy alloy with gigapascal yield strength [J]. Proceedings of the National Academy of Sciences of the United States of America, 2018, 115: 7224−7229.

[20] WANG Yan-fei, WANG Ming-sai, FANG Xiao-tian, GUO Feng-jiao, LIU Han-qing, SCATTERGOOD R O, HUANG Chong-xiang, ZHU Yun-tian. Extra strengthening in a coarse/ultrafine grained laminate: Role of gradient interfaces [J]. International Journal of Plasticity, 2019, 123: 196−207.

[21] SHI Pei-jian, REN Wei-li, ZHENG Tian-xiang, REN Zhong-ming, HOU Xue-ling, PENG Jian-chao, HU Peng-fei, GAO Yan-fei, ZHONG Yun-bo, LIAW P K. Enhanced strength-ductility synergy in ultrafine-grained eutectic high-entropy alloys by inheriting microstructural lamellae [J]. Nature Communications, 2019, 10: 489.

[22] ZHU Yun-tian, WU Xiao-lei. Perspective on hetero-deformation induced (HDI) hardening and back stress [J]. Materials Research Letters, 2019, 7: 393−398.

[23] SHI Pei-jian, ZHONG Yun-bo, LI Yi, REN Wei-li, ZHENG Tian-xiang, SHEN Zhe, YANG Bing, PENG Jian-chao, HU Peng-fei, ZHANG Yong, LIAW P K, ZHU Yun-tian. Multistage work hardening assisted by multi-type twinning in ultrafine-grained heterostructural eutectic high-entropy alloys [J]. Materials Today, 2020, 41: 62−71.

[24] TAN Chang-sheng, SUN Qiao-yan, XIAO Lin, ZHAO Yong-qing, SUN Jun. Cyclic deformation and microcrack initiation during stress controlled high cycle fatigue of a titanium alloy [J]. Materials Science and Engineering: A, 2018, 711: 212−222.

[25] LIU Cong-hui, XU Xu, SUN Tian-zhu, THOMAS R, da FONSECA J Q, PREUSS M. Microstructural effects on fatigue crack initiation mechanisms in a near-alpha titanium alloy [J]. Acta Materialia, 2023, 253: 118957.

[26] ZHANG Sai-fei, ZENG Wei-dong, ZHAO Qin-yang, GAO Xiong-xiong, WANG Qing-jiang. High cycle fatigue of isothermally forged Ti−6.5Al−2.2Mo−2.2Zr−1.8Sn−0.7W−0.2Si with different microstructures [J]. Journal of Alloys and Compounds, 2016, 689: 114−122.

[27] DICHTL C, ZHANG Zhen-bo, GARDNER H, BAGOT P, RADECKA A, DYE D, THOMAS M, SANDALA R, da FONSECA J Q, PREUSS M. Element segregation and $\alpha 2$ formation in primary α of a near-α Ti-alloy [J]. Materials Characterization, 2020, 164: 110327.

[28] CHEN Kui-wai, PAN Su-ping, LIU Hui-qun, JIANG Yong. Effect of α phase morphology on fatigue crack growth behavior of Ti−5Al−5Mo−5V−1Cr−1Fe alloy [J]. Transactions of Nonferrous Metals Society of China, 2020, 30: 2459−2471.

[29] UEKI S, MINE Y, CHIU Y L, BOWEN P, TAKASHIMA K. Effects of crystallographic orientation and lamellar configuration on fatigue crack propagation in single-colony structures of Ti−6Al−4V alloy: Alternating shear crack growth vs. damage accumulation crack propagation [J]. Materials Science and Engineering: A, 2024, 890: 145885.

[30] WANG Tong-bo, LI Bo-long, WANG Zhen-qiang, NIE Zuo-ren. A microstructure with improved thermal stability and creep resistance in a novel near-alpha titanium alloy [J]. Materials Science and Engineering: A, 2018, 731: 12−20.

[31] LONARDELLI I, GEY N, WENK H R, HUMBERT M, VOGEL S C, LUTTEROTTI L. In situ observation of texture evolution during $\alpha \rightarrow \beta$ and $\beta \rightarrow \alpha$ phase transformations in titanium alloys investigated by neutron diffraction [J]. Acta Materialia, 2007, 55: 5718−5727.

[32] WENG Han-bo, HUANG Sen-sen, YANG Jie, QI Min, MA Ying-jie, WANG Yu-xiang, XU Dao-kui, QIU Jian-ke, LEI Jia-feng, GONG Bin, YANG Rui. Mechanical properties anisotropy of Ti−6Al−4V alloy fabricated by β forging [J]. Transactions of Nonferrous Metals Society of China, 2023, 33: 3348−3363.

[33] WANG Yin-ming, CHEN Ming-wei, ZHOU Feng-hua, MA E. High tensile ductility in a nanostructured metal [J]. Nature, 2002, 419: 912−915.

[34] WU Chuan, YANG He, LI Hong-wei, FAN Xiao-guang. Static coarsening of titanium alloys in single field by cellular automaton model considering solute drag and anisotropic mobility of grain boundaries [J]. Chinese Science Bulletin, 2012, 57: 1473−1482.

[35] MAHENDER T, ANANTHA PADMANABAN M R, BALASUNDAR I, RAGHU T. On the optimization of temperature and cooling rate to maximize strength and ductility of near α titanium alloy IMI 834 [J]. Materials Science and Engineering: A, 2021, 827: 142052.

[36] ZHOU Yu, WANG Ke, LI Hong-hui, WEN Xin, XIN Ren-long. Effect of content and configuration of equiaxed α and lamellar α on deformation mechanism and tensile properties of a near-α titanium alloy [J]. Materials Science and Engineering: A, 2023, 877: 145192.

[37] GAO Peng-fei, QIN G, WANG Xian-xian, LI Yan-xi, ZHAN Mei, LI Guang-jun, LI Jin-shan. Dependence of mechanical properties on the microstructural parameters of TA15 titanium alloy with tri-modal microstructure [J]. Materials Science and Engineering: A, 2019, 739: 203−213.

[38] LIU Zhi-ying, LI Ren-kai, CHEN Dao-lun, SUN Yu, HE Bei, ZOU Yu. Enhanced tensile ductility of an additively manufactured near-α titanium alloy by microscale shear banding [J]. International Journal of Plasticity, 2022, 157:

103387.
[39] SU Yu, FAN Hao-yu, YOU Feng-Hai, KONG Fan-tao, WANG Xiao-peng, CHEN Yu-yong. Improved tensile properties of a novel near-α titanium alloy via tailoring microstructure by hot-rolling [J]. Materials Science and Engineering: A, 2020, 790: 139588.
[40] NARAYANA P L, KIM S W, HONG J K, REDDY N S, YEOM J T. Tensile properties of a newly developed high-temperature titanium alloy at room temperature and 650 °C [J]. Materials Science and Engineering: A, 2018, 718: 287−291.
[41] WANG Si-jia, YANG Ji-xin, SUN Jian-fei, SHU Wen-xiang, YANG Hai-bin, NGAN A H W, HUANG Yong-jiang. Tensile properties of Ti6.5Al2Zr1Mo1V titanium alloy fabricated via electron beam selective melting at high temperature [J]. Materials Science and Engineering: A, 2023, 888: 145806.
[42] LI Wen-yuan, CHEN Zhi-yong, LIU Jian-rong, ZHU Shao-xiang, SUI Guo-xin, WANG Qing-jiang. Rolling texture and its effect on tensile property of a near-α titanium alloy Ti60 plate [J]. Journal of Materials Science & Technology, 2019, 35: 790−798.
[43] SU Yu, KONG Fan-tao, YOU Feng-Hai, WANG Xiao-peng, CHEN Yu-yong. The high-temperature deformation behavior of a novel near-α titanium alloy and hot-forging based on the processing map [J]. Vacuum, 2020, 173: 109135.
[44] WANG Yong-ling, SONG Xiao-yun, MA Wen, ZHANG Wen-jing, YE Wen-jun, HUI Song-xiao. Microstructure and tensile properties of Ti-62421S alloy plate with different annealing treatments [J]. Rare Metals, 2014, 37: 568−573.
[45] YANG Mu-xin, PAN Yue, YUAN Fu-ping, ZHU Yun-tian, WU Xiao-lei. Back stress strengthening and strain hardening in gradient structure [J]. Materials Research Letters, 2016, 4: 145−151.
[46] LIU Xiao-long, XUE Qi-qi, WANG Wei, ZHOU L L, JIANG Ping, MA Han-song, YUAN Fu-ping, WEI Yue-guang, WU Xiao-lei. Back-stress-induced strengthening and strain hardening in dual-phase steel [J]. Materialia, 2019, 7: 100376.
[47] ZHU Yun-tian, WU Xiao-lei. Heterostructured materials [J]. Progress in Materials Science, 2023, 131: 101019.
[48] MUGHRABI H. Dislocation wall and cell structures and long-range internal stresses in deformed metal crystals [J]. Acta Metallurgica, 1983, 31: 1367−1379.
[49] SINCLAIR C W, SAADA G, EMBURY J D. Role of internal stresses in co-deformed two-phase materials [J]. Philosophical Magazine, 2006, 86: 4081−4098.
[50] GIBELING J G, NIX W D. A numerical study of long range internal stresses associated with subgrain boundaries [J]. Acta Metallurgica, 1980, 28: 1743−1752.
[51] SHI Xiao-hui, ZHANG Qi, JING Zhen, FAN Zhi-yuan, LIU Jiang-lin, QIAO Jun-wei. Strengthening behavior and model of ultra-high strength Ti−15Mo−2.7Nb−3Al−0.2Si titanium alloy [J]. Transactions of Nonferrous Metals Society of China, 2024, 34: 1136−1149.
[52] LUO Hang, XU Ping-wei, LIN Ting-yi, ZHOU Lei, LUO Ming-lang, JIANG Zi-hao, LIANG Yi-long, LIANG Yu. Effect of α_p/β trans interfacial microstructure on tensile property and deformation behavior in Ti6242 alloys [J]. Materials Science and Engineering: A, 2022, 844: 143149.
[53] ZHU Wen-guang, MA Chi, ZHANG Cong-hui, HU Kun, ZENG Xiang-kang. Fatigue crack propagation behavior in Ti−6Al−4V alloy with surface gradient structure fabricated by high-energy shot peening [J]. Transactions of Nonferrous Metals Society of China, 2023, 33: 3003−3016.
[54] WILLIAMS J C, BAGGERLY R G, PATON N E. Deformation behavior of HCP Ti−Al alloy single crystals [J]. Metallurgical and Materials Transactions A-physical Metallurgy and Materials Science, 2002, 33: 837−850.

近α钛合金异质结构的结构特征、拉伸性能和室温高周疲劳性能

胡继飞[1]，亓 鹏[2]，魏 午[1]，李伯龙[1]，王同波[2]，尹嘉明[3]，聂祚仁[1]

1. 北京工业大学 新型功能材料教育部重点实验室，北京 100124；
2. 中铝科学技术研究院有限公司，北京 102209；
3. 航天材料与加工技术研究所，北京 100076

摘 要：通过对具有双态组织的初始钛合金依次进行热轧、退火和时效处理，制备由细长的初生 α 晶粒和尺寸为 670 nm 的次生 α 晶粒组成的异质结构。具有异质结构的钛合金的高强度主要归因于异质变形诱导强化和位错强化。通过结合短时高温热处理，实现室温和 650 ℃高温下屈服强度和伸长率的协同提高，断裂伸长率比初始合金分别提高了 36.7%和 130.4%。具有单一滑移系统的几何必要位错在相边界处堆积以及更长的位错有效滑移长度是实现伸长率显著提高的原因。合金具有更好的抗疲劳裂纹萌生效果归因于其层片双态组织中由多个初生 α 晶粒组成的细长初生 α 相。

关键词：钛合金；异质结构；延展性；高温变形；异质变形诱导强化

(Edited by Xiang-qun LI)